Available online at www.sciencedirect.com
ScienceDirect
Trans. Nonferrous Met. Soc. China 32(2022) 2003−2018
Transactions of Nonferrous Metals Society of China
www.tnmsc.cn

SPH−FEM simulations of microwave-treated basalt strength

Chun YANG[1,2,3], Ferri HASSANI[2], Ke-ping ZHOU[1,3], Feng GAO[1,3], Ameen TOPA[4,5]

1. School of Resources and Safety Engineering, Central South University, Changsha 410083, China;
2. Department of Mining and Materials Engineering, McGill University, 3450 University, Frank Dawson Adams Bldg., Montreal, QC H3A 0E8, Canada;
3. Research Center for Mining Engineering and Technology in Cold Regions, Central South University, Changsha 410083, China;
4. Institute of Transportation Infrastructure, Universiti Teknologi PETRONAS, Seri Iskandar, Perak 32610, Malaysia;
5. Department of Maritime Technology, University Malaysia Terengganu, Kuala Terengganu 21300, Malaysia

Received 7 April 2021; accepted 17 August 2021

Abstract: Microwave precondition has been highlighted as a promising technology for softening the rock mass prior to rock breakage by machine to reduce drill bit/cutter wear as well as inverse production rate. To numerically explore the effect of numerical parameters on rock static strength simulation, and determine the numerical mechanical parameters of microwave-treated basalts for future drilling and cutting simulations, numerical models of uniaxial compression strength (UCS) and Brazilian tensile strength (BTS) were established with the coupling of smoothed particle hydrodynamics and finite element method (SPH−FEM). To eliminate the large rock strength errors caused by microwave-induced damage, the cohesion and internal friction angle of microwave-treated basalt specimens with the same microwave treatment parameters were calibrated based on a linear Mohr−Coulomb theory. Based on parametric sensitivity analysis of SPH simulation of UCS and BTS, experimental UCS and BTS values were simultaneously captured according to the same set of calibrated cohesion and internal friction angle data, and the UCS modeling results are in good agreement with experimental tests. Furthermore, the effect of microwave irradiation parameter on the basalt mechanical behaviors was evaluated.

Key words: microwave irradiation; microwave-assisted rock breakage; rock mechanics; smoothed particle hydrodynamics (SPH); parametric sensitivity analysis

1 Introduction

Rock breakage strongly affects the efficiency and safety of geotechnical engineering operations. Microwave heating is a promising method to soften hard rocks prior to breakage (Fig. 1). Static strength tests show that microwaves can weaken specimens of rock containing microwave-absorbing minerals (to varying degrees, depending on the mineral types, content, and spatial distribution in the rock) [1,2]. In the field, the rock mass may subject dynamic impacts [3], and dynamic tests (e.g., drop-weight impact and split Hopkinson pressure bar tests) indicate that microwaves can also greatly weaken rock dynamic strength [4−6]. Given that hard rock promotes serious drill bit/cutter wear on rock breakage machines, microwave-assisted rock breakage could be combined with tunnel boring or other rock excavation machines to improve rock cutting/drilling efficiency and decrease wear, thus extending machine service life [7,8].

Bit performance can be empirically assessed in the laboratory using scratch tests, Schmidt hammer

Corresponding author: Feng GAO, E-mail: csugaofeng@csu.edu.cn
DOI: 10.1016/S1003-6326(22)65926-0

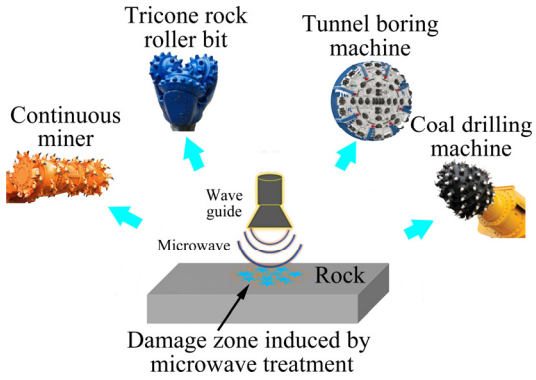

Fig. 1 Concept of microwave-assisted mechanical rock breakage

tests, or drilling tests with small rock specimens. However, the applicability of bench-scale results to the field is limited: the microwave power of laboratory microwave equipment is relatively low, which limits the microwave penetration into the rock specimen, and the microwave cavity is small, which means that the microwave-treated rocks would not meet the dimensional requirements for linear cutting tests [9]. To overcome this limitation, microwave irradiation system with an open-ended waveguide is used to perform irradiation test. Microwave irradiating multiple spots at the rock block surface induced a large-scaled network of cracks, which makes it feasible to conduct linear cutting test for the microwave-treated rock block [10]. However, large scale rock experimental test involves tedious preparation procedure, and it is unrepeatable due to the randomly distributed cracks [11].

As a highly efficient and low-cost approach, numerical simulation could provide new insights on disc cutter performance on a microwave-treated rock mass. The explicit dynamic analysis software, LS-DYNA, has been widely used for rock simulation [12]. In LS-DYNA code, the smoothed particle hydrodynamics (SPH) approach can simulate large deformation such as rock debris motion caused by cutting or drilling [13,14]. Thus, the SPH model of microwave-treated rock is presented in this study. The first step is to determine the appropriate mechanical parameters of the microwave-treated rock and numerical model. During microwave-assisted rock breakage, rock damage is induced by the uneven distribution of thermal stress, which is governed by the dielectric properties of minerals in the rock [15]. Because rock is heterogeneous, microwave-induced cracks propagate randomly, enhancing the inhomogeneity of rock [16]. Although the digital rock technique can generate a detailed model with cracks in numerical simulation, model dimensions may not meet the needs for cutting or drilling modeling [17]. Furthermore, the relative position of the cutter/bit and the rock specimen with cracks affects cutting performance, and thus it is not possible to compare numerical results among experimental groups [18]. It is known that rock strength strongly influences rock fracturing behavior; in particular, tensile strength governs most rock failures [19−21]. Therefore, a compromise is to match experimental uniaxial compression (UCS) and Brazilian tensile strength (BTS) with a homogeneous numerical model and make the numerical parameters governing rock deformation consistent with empirical results.

The focus of this study is to numerically explore the effect of SPH parameters on rock static strength simulation, and determine the numerical mechanical parameters of microwave-treated basalts. The parametric study results are expected to lay the foundation for numerically exploring the mechanical breaking behavior of microwave-damaged rock in geotechnics, such as future cutting and drilling modeling of microwave-treated basalt. This work uses detailed published experimental data from LU et al [22,23] on UCS, BTS, and conventional triaxial compressive strength (CTCS) of microwave-treated basalts. A hybrid algorithm SPH-FEM is employed to simulate the UCS and BTS of microwave-treated basalt with LS-DYNA code. Furthermore, the effect of microwave irradiation parameter on the basalt mechanical behaviors is evaluated.

2 Principles of SPH method

2.1 SPH formulation

SPH algorithm was proposed by GINGOLD and MONAGHAN [24] and LUCY [25] in 1977, primarily for astrophysics applications. Subsequent improvements by various researchers have made SPH an efficient mesh-free particle method that is widely applied to simulating the mechanics of continuum media, such as solid mechanics and fluid flows [26,27]. As a Lagrangian method, the SPH method is based on the hypothesis that the problem

domain can be divided into a set of discrete moving particles with independent quality and space (Fig. 2). Therefore, unlike the finite element method (FEM), no element distortion occurs in a SPH model [28]. Parameters such as density, stress distribution, strain, temperature history, velocity, and deformation are estimated from the weighted mean size of the mathematical nodes over neighboring nodes through interpolation functions known as kernels (Fig. 2).

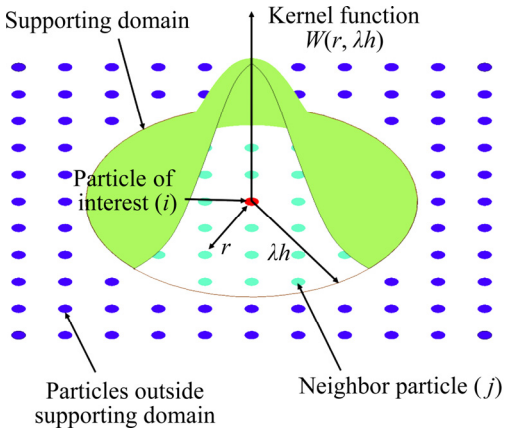

Fig. 2 Particle interactions in SPH within influence domain governed by kernel functions

The scalar function $f(x)$ is continuous over the whole support domain, and can be written as

$$f(\boldsymbol{x})=\int f(\boldsymbol{x}')\delta(\boldsymbol{x}-\boldsymbol{x}')\mathrm{d}\boldsymbol{x}' \tag{1}$$

where $\boldsymbol{x}$ is the position vector, and $\delta(\boldsymbol{x}–\boldsymbol{x}')$ is the Dirac delta function, given as

$$\delta(\boldsymbol{x}-\boldsymbol{x}')=\begin{cases}+\infty, \boldsymbol{x}=\boldsymbol{x}'\\ 0, \boldsymbol{x}\neq\boldsymbol{x}'\end{cases} \tag{2}$$

Dirac delta function must have a property that its integral over the entire volume equals unity.

If the Dirac delta function is replaced by smoothing (kernel) function $W(\boldsymbol{x}–\boldsymbol{x}', h)$, the kernel approximation is expressed as

$$\langle f(\boldsymbol{x})\rangle=\int f(\boldsymbol{x}')\,W(\boldsymbol{x}-\boldsymbol{x}', h)\,\mathrm{d}\boldsymbol{x}' \tag{3}$$

where h is smoothing length.

The kernel function should satisfy the Dirac delta function as smoothing length approaches zero. Among the four kernel functions (cubic spline, quartic, quadratic spline, and quintic spline) available in LS-DYNA code, the default cubic spline kernel function is applicable to most simulations. It is expressed as

$$W(r,h)=\alpha_{\mathrm{D}}\times\begin{cases}1-\dfrac{2}{2}q^2+\dfrac{3}{4}q^3, 0\le q\le 1\\ \dfrac{1}{4}(2-q)^3, 1\le q\le 2\\ 0, q\ge 2\end{cases} \tag{4}$$

where q is the ratio of particle spacing (r) to smoothing length (h); α_{D} equals $1/(\pi h^3)$ in a three-dimensional domain.

If the volume, ΔV_j, of particle j is introduced into Eq. (3), the computational domain can be discretized into a finite number of particles based on the following equation:

$$\langle f(x_i)\rangle\approx\sum_j\frac{m_j}{\rho_j}f(x_j)W(|x_i-x_j|,h) \tag{5}$$

where ρ_j and m_j denote the density and mass of particle j, respectively; j = 1, 2, ⋯, N, and N is the number of particles in the support domain of particle i; x_i and x_j represent the positions of particles i and j, respectively.

2.2 Governing equations

The conservation laws of mass, momentum, and energy are given by Eqs. (6), (7), and (8), respectively [29]:

$$\frac{\mathrm{d}\rho_i}{\mathrm{d}t}=\sum_{j=1}^{N}m_j v_{ij}^{\boldsymbol{\beta}}\frac{\partial W_{ij}}{\partial x_i^{\boldsymbol{\beta}}} \tag{6}$$

$$\frac{\mathrm{d}v_i^{\boldsymbol{\alpha}}}{\mathrm{d}t}=\sum_{j=1}^{N}m_j\left(\frac{\boldsymbol{\sigma}_i^{\boldsymbol{\alpha\beta}}}{\rho_i^2}+\frac{\boldsymbol{\sigma}_j^{\boldsymbol{\alpha\beta}}}{\rho_j^2}\right)\frac{\partial W_{ij}}{\partial x_i^{\boldsymbol{\beta}}} \tag{7}$$

$$\frac{\mathrm{d}e_i}{\mathrm{d}t}=\frac{1}{2}\sum_{j=1}^{N}m_j\left(\frac{\boldsymbol{\sigma}_i^{\boldsymbol{\alpha\beta}}}{\rho_i^2}+\frac{\boldsymbol{\sigma}_j^{\boldsymbol{\alpha\beta}}}{\rho_{\mathrm{j}}^2}\right)v_{ij}^{\boldsymbol{\alpha}}\frac{\partial W_{ij}}{\partial x_i^{\boldsymbol{\beta}}} \tag{8}$$

where $\boldsymbol{\alpha}$ and $\boldsymbol{\beta}$ are both space vectors; ρ_i and ρ_j are the densities of particles i and j, respectively; $x_i^{\boldsymbol{\beta}}$ is the coordinate component of $\boldsymbol{x}$ along $\boldsymbol{\beta}$; W_{ij} indicates the smoothing function between particles i and j; $v_{ij}^{\boldsymbol{\alpha}}$ and $v_{ij}^{\boldsymbol{\beta}}$ represent the velocities for particle i relative to particle j along $\boldsymbol{\alpha}$ and $\boldsymbol{\beta}$, respectively; m_j is the mass of particle j; $v_i^{\boldsymbol{\alpha}}$ and $v_j^{\boldsymbol{\alpha}}$ denote the velocity components of particles i and j along $\boldsymbol{\alpha}$, respectively; $\boldsymbol{\sigma}_i^{\boldsymbol{\alpha\beta}}$ and $\boldsymbol{\sigma}_j^{\boldsymbol{\alpha\beta}}$ are the total stress tensors of particles i and j, respectively; e_i is the internal energy of particle i; t is time.

Many numerical solutions of the continuum equations exhibit large unphysical oscillations near shocks due to the omission of dissipative terms [30].

To deal with this, artificial viscosity is introduced to SPH governing equations, which is able to not only eliminate the unphysical oscillation, but also prevent the penetration of SPH particles [31]. In LS-DYNA code, the Monaghan-type artificial viscosity is used (Eq. (9)):

$$\Pi_{ij}=\begin{cases}\dfrac{-\alpha_1\bar{c}_{ij}\mu_{ij}+\beta_1\mu_{ij}^2}{\bar{\rho}_{ij}}, & v_{ij}x_{ij}<0\\ 0, & v_{ij}x_{ij}\geq 0\end{cases} \tag{9}$$

where α_1 and β_1 are input constants and c is the speed of sound in the material and

$$\mu_{ij}=\frac{h_{ij}v_{ij}x_{ij}}{|x_{ij}|^2+\mu^2}$$

$$\bar{c}_{ij}=0.5(c_i+c_j)$$

$$\bar{\rho}_{ij}=0.5(\rho_i+\rho_j)$$

$$h_{ij}=0.5(h_i+h_j)$$

$$\mu=0.1h_{ij}$$

The parametric study indicated that numerical results are more sensitive to the value of α_1 than β_1. Thus, it is recommended that the user set both α_1 and β_1 to be 1 on *CONTROL_BULK_VISCOSITY. Fluid material simulation generally needs a much small value for β_1.

Therefore, Eqs. (7) and (8) can be rewritten as Eqs. (10) and (11), respectively:

$$\frac{\mathrm{d}v_i^{\alpha}}{\mathrm{d}t}=\sum_{j=1}^{N}m_j\left(\frac{\sigma_i^{\alpha\beta}}{\rho_i^2}+\frac{\sigma_j^{\alpha\beta}}{\rho_j^2}+\Pi_{ij}\right)\frac{\partial W_{ij}}{\partial x_i^{\beta}} \tag{10}$$

$$\frac{\mathrm{d}e_i}{\mathrm{d}t}=\frac{1}{2}\sum_{j=1}^{N}m_j\left(\frac{\sigma_i^{\alpha\beta}}{\rho_i^2}+\frac{\sigma_j^{\alpha\beta}}{\rho_j^2}+\Pi_{ij}\right)v_{ij}^{\alpha}\frac{\partial W_{ij}}{\partial x_i^{\beta}} \tag{11}$$

2.3 Solution procedures

The SPH calculation cycle in LS-DYNA (Fig. 3) is similar to that for computation in FEM except some steps involve use of kernel approximations as discussed above. A specific particle searches for neighbors within a support domain. In each time step, kernel approximations are used to estimate (1) the density and strain rates of each particle using the spatial derivatives of velocities and (2) forces of each particle from the spatial derivatives of stresses [32].

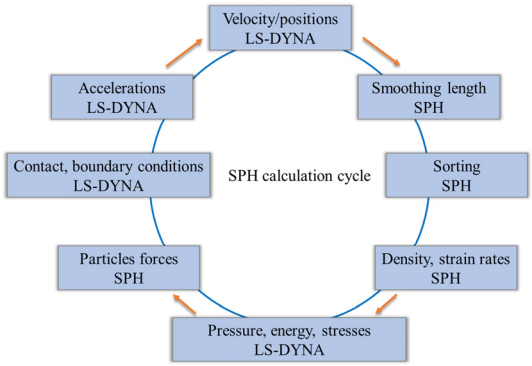

Fig. 3 SPH calculation cycle in LS-DYNA

3 Numerical calibration

3.1 Rock physical parameter calibration

Generally, multimode cavity is more efficient to process products in bulk than single-mode cavity in terms of heating efficiency and uniformity. Thus, a CM-06S multimode cavity at 2.45 GHz was used in microwave heating test. The effect of water content on basalt microwave response is not considered in the experimental tests. Preliminary experiments are conducted to determine the proper microwave treatment parameters, which showed that at applied powers of 1, 3 and 5 kW, the standard cylindrical basalt specimens were broken and damaged after about 320, 110, and 50 s, respectively. Thus, in order to ensure that the microwave-treated basalt specimens meet the needs for mechanical behavior test, the microwave treatment duration should be less than aforementioned time. Microwave heating tests were conducted on triplicate basalt specimens and microwave was at three power levels for various treatment time (Table 1). The control group did not receive microwave treatment. All specimens were subjected to UCS and BTS tests following the procedures recommended by International Society for Rock Mechanics and Rock Engineering [33]. In addition, cylindrical specimens of the 5 kW treatment group were prepared for CTCS tests under three confining pressures to determine the friction angle and cohesion (Table 1). Linear regression analysis was used to determine relationships between basalt strength and microwave treatment time at the three power levels (Table 2).

It is evident from Table 2 that there was a strong negative relationship between basalt static

Table 1 Experimental design for microwave treatment and strength testing of basalt specimens

Test	Specimen shape	Specimen size	Microwave power/kW	Exposure time/s	Confining pressure/MPa
UCS	Cylinder	*d*50 mm × 100 mm	1	60, 180, 300	0
			3	30, 60, 90	0
			5	10, 20, 30	0
BTS	Disc	50 mm × 50 mm	1	60, 180, 300	0
			3	30, 60, 90	0
			5	10, 20, 30	0
CTCS	Cylinder	50 mm × 100 mm	5	10, 20, 30	10
			5	10, 20, 30	30
			5	10, 20, 30	50

Table 2 Relationships between deformation parameters and microwave irradiation time

Deformation parameter	Microwave power/kW	Regression equation	R^2
UCS	1	UCS = 278.18−0.26*t*	0.92
	3	UCS = 282.18−0.97*t*	0.94
	5	UCS = 280.80−2.49*t*	0.99
BTS	1	BTS = 15.60−0.02*t*	0.94
	3	BTS = 15.43−0.06*t*	0.93
	5	BTS = 15.49−0.25*t*	0.96
Poisson's ratio	1	υ = 0.28−0.00009*t*	0.62
	3	υ = 0.28−0.0006*t*	0.98
	5	υ = 0.28−0.002*t*	0.89
Elastic modulus	1	*E* = 95.64−0.06*t*	0.96
	3	*E* = 97.07−0.26*t*	0.97
	5	*E* = 92.43−0.58*t*	0.88
Friction angle	5	ϕ =50.38−0.06*t*	0.73
Cohesion	5	*c* = 53.07−0.39*t*	0.79

strength (UCS and BTS) and microwave treatment time. Further, the magnitude of the negative slope increased with microwave power level. The same pattern was observed for the rock deformation indicators (Poisson's ratio and elastic modulus). At the highest microwave power level, the cohesion and friction angle were also negatively related to treatment time. The fitted physical and mechanical parameters based on the regression equations in Table 2 are listed in Table 3.

3.2 Numerical parameter calibration

Several material models in LS-DYNA code are available for modeling rock and concrete materials deforming under different loading conditions, such as *MAT_MOHR_COULOMB, *MAT_PLASTIC_KINEMATIC, *MAT_BRITTLE_DAMAGE, *MAT_JOHNSON_HOLMQUIST_CONCRETE, *MAT_CSCM, and *MAT_RHT [34]. However, numerical parameters for some material models involve dozens of physical parameters, which need to be determined by numerous experimental tests. Thus, it is very cumbersome to validate the numerical parameters. In geotechnical engineering, the Mohr-Coulomb model is the most common model in the context of geomaterials. It postulates a linear relationship between shear strength on a plane and the normal stress acting on it. This can be represented by plotting Mohr's circle for states of stress at failure in terms of the maximum and minimum principal stresses (Fig. 4). The linear Mohr−Coulomb model can be written as

$$\tau=c+\sigma\tan\phi \tag{12}$$

where τ is the shear stress, σ is the normal stress, c is the cohesion of the material, and ϕ is internal friction angle.

The linear Mohr−Coulomb model is included in LS-DYNA code. All basalt parameters obtained above matched very well with the requirements for the inputting numerical parameters for the Mohr−Coulomb model. Therefore, *MAT_MOHR_COULOMB material model was implemented in this numerical investigation.

Rock material is anisotropic because it contains natural flaws, such as joints, pores, and cracks [35]. In the numerical model, rock was simplified as a homogeneous material. Microwave treatment damaged rock specimens (e.g., formation

Table 3 Fitted basalt physical and mechanical parameters

Group	Microwave power/kW	Exposure time/s	Elastic modulus/GPa	Poisson's ratio	Cohesion/ MPa	Internal friction angle/(°)	UCS/ MPa	BTS/ MPa
M1	0	0	97.07	0.28	–	–	282.18	15.43
M2	1	60	94.04	0.27	–	–	262.58	14.40
M3	1	180	86.84	0.26	–	–	231.38	12.00
M4	1	300	79.64	0.25	–	–	200.18	9.60
M5	3	30	89.27	0.26	–	–	253.08	13.63
M6	3	60	81.47	0.24	–	–	223.98	11.83
M7	3	90	73.67	0.23	–	–	194.88	10.03
M8	5	10	86.54	0.26	49.17	49.78	255.90	12.99
M9	5	20	80.65	0.24	45.27	49.18	231.00	10.49
M10	5	30	74.76	0.22	41.37	48.58	206.10	7.99

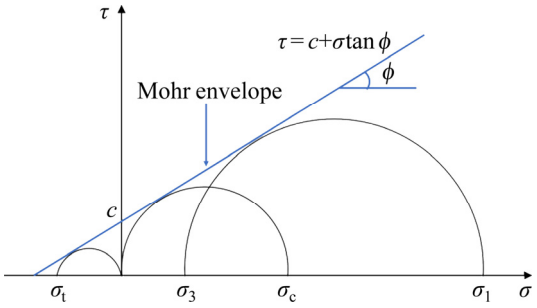

Fig. 4 Linear Mohr−Coulomb model

of irregular cracks in cylindrical specimens; Fig. 5), which would likely enhance the variation in experimental results. Given that the physical parameters from each testing group can only represent the physical and mechanical properties of the corresponding test specimen, before inputting the experimental results into the modeling software, calibration was required.

Compression is assumed to be positive in the following discussion. In the triaxial stress state, Mohr-Coulomb failure surface can be expressed as

$$\frac{\sigma_1-\sigma_3}{2}=\frac{\sigma_1+\sigma_3}{2}\sin\phi+c\cos\phi \tag{13}$$

where σ_1 and σ_3 denote the major and minor principal stress, respectively.

In a pure compression stress state, σ_1=UCS and σ_3=0, and thus we have

$$\mathrm{UCS}=\frac{2c\cos\phi}{1-\sin\phi} \tag{14}$$

In pure tension stress state, σ_1=0 and $-\sigma_3$=BTS (BTS denotes tensile strength in the following discussion), and thus we have

$$\mathrm{BTS}=\frac{2c\cos\phi}{1+\sin\phi} \tag{15}$$

Therefore, for a linear Mohr−Coulomb failure criterion, the UCS and BTS can be predicted by Eqs. (14) and (15) when the cohesion and internal friction angle are known. For the 5 kW testing group, the cohesion and internal friction angle were determined by CTCS tests. When the fitted experimental cohesion and internal friction angle of Group M8 (Table 3) are brought into Eqs. (14) and (15), the predicted UCS and BTS are 268.58 and 36.01 MPa, respectively, which differs from the fitted experimental UCS and BTS (255.90 and 12.99 MPa, respectively). This discrepancy has a large impact on the shear stress value predicted by the linear Mohr−Coulomb model. It should be noted that most rock engineering failure is governed by tensile strength. In order to make the experimental UCS and BTS valid in numerical simulations, the cohesion and internal friction angles were calibrated based on Eqs. (14) and (15) via back-calculation (Table 4).

4 UCS modeling and results

4.1 Numerical boundary conditions

The numerical UCS model consisting of an upper platen, a lower platen and a rock cylinder (d50 mm × 100 mm) was simulated in LS-DYNA by SPH particles (Fig. 6). Because the implementation of boundary conditions and computational efficiency are poor in SPH relative to

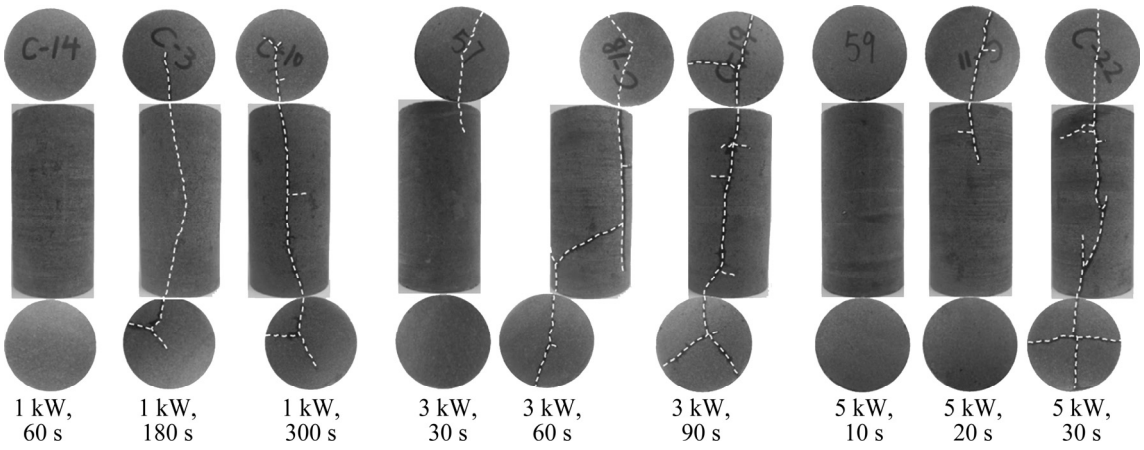

Fig. 5 Crack patterns on surfaces of cylindrical microwave-treated basalt specimens [22]

Table 4 Calibrated basalt physical parameters

Group	Cohesion/MPa	Internal friction angle/(°)
M1	32.99	63.68
M2	30.75	63.64
M3	26.35	64.34
M4	21.92	65.30
M5	29.37	63.87
M6	25.74	64.11
M7	22.11	64.44
M8	28.83	64.61
M9	24.61	65.94
M10	20.29	67.72

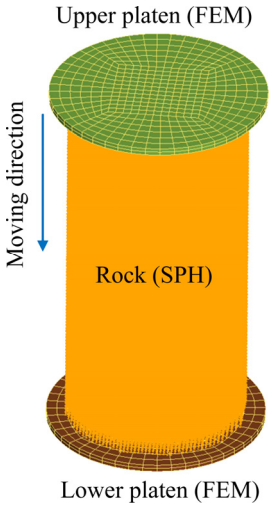

Fig. 6 Numerical UCS model

FEM, the two platens were modeled by a finite element rigid body: the upper platen is prescribed at a constant vertical velocity, and the lower platen is constrained. In order to get the real section area of the cylindrical model, the SPH particle model was converted from finite element in LS-PREPOST software. The average axial stress was calculated by dividing the contact forces on the interface between the upper platen and rock by the real cross-sectional area of the rock cylinder.

To couple FEM and SPH, it is crucial to calculate the forces exchanged between elements and particles near the coupling interfaces. In the interface between the SPH particles and FEM model, finite element nodes are regarded as background particles that have the same attributions as SPH particles (Fig. 7). The mass, position, velocity, and stress of the background particles are in accordance with finite element nodes. The interaction between platens and SPH cylinder is defined with the contact algorithm *CONTACT_AUTOMATIC_NODES_TO_SURFACE, where the two platens are treated as the “master” and the SPH particles of rock are treated the “slave” [37,38].

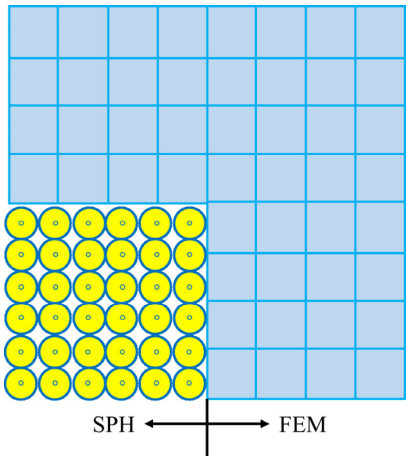

Fig. 7 Attachment algorithm for coupled SPH−FEM method [36]

4.2 Effect of loading speed

LS-DYNA is a multi-physics solver comprising an implicit solver and explicit solver. The implicit solver provides both linear and nonlinear analysis options, including the choice of static or various dynamic solution schemes, especially the long-term mechanical response. Static rock strength tests are relatively time-consuming due to the low loading speed; thus, the implicit solution might be most suitable. However, LS-DYNA implicit analysis requires many implicit numerical parameters to reach convergence, and it takes a great deal of time to determine optimal parameters. The explicit solver is intended to quickly simulate highly dynamic problems. Quasi-static loading in explicit analysis enhances the loading speed to save simulation time. This study uses numerical simulation of static rock experiments with a quasi-static loading technique in the explicit solver in LS-DYNA.

Rock is a rate-dependent material: its mechanical properties change with loading rate. However, it is shown that the loading rate only influences the mechanical properties of rock above a threshold loading rate [39]. A series of preliminary simulations were conducted to determine the optimum loading speed for UCS modeling. The physical and mechanical parameters of Group M1 (untreated control) were used for the parametric sensitivity analysis. Five nominal strain rates were applied for each model. The normal contact force increases with loading speed (Fig. 8). At nominal strain rates from 0.001 to 0.01 s^{-1}, the force−displacement curves are similar, but at nominal strain rates above 0.01 s^{-1}, the displacement is clearly higher for a given force. Further, oscillations are evident, which are caused by high-speed impacts. The force−displacement curves indicate that a nominal strain rate below 0.01 s^{-1} is acceptable for UCS modeling with a quasi-static loading simulation. Given that lower nominal strain rates require a longer simulation time, a constant nominal strain rate of 0.01 s^{-1} was selected for UCS modeling.

4.3 Effect of particle spacing

The normal peak stress was calculated to assess the effect of particle spacing since it influences the accuracy of the numerical results and thus requires careful examination and consideration to balance accuracy and simulation time. Five numerical models with SPH particle spacings of 5, 4, 3, 2, and 1 mm were used to evaluate particle spacing sensitivity (Fig. 9), with corresponding real section areas of the SPH cylinder of 14.25, 15.28, 16.00, 17.48, and 18.57 cm^2, respectively. According to SPH theory, the optimal distribution of particles is even.

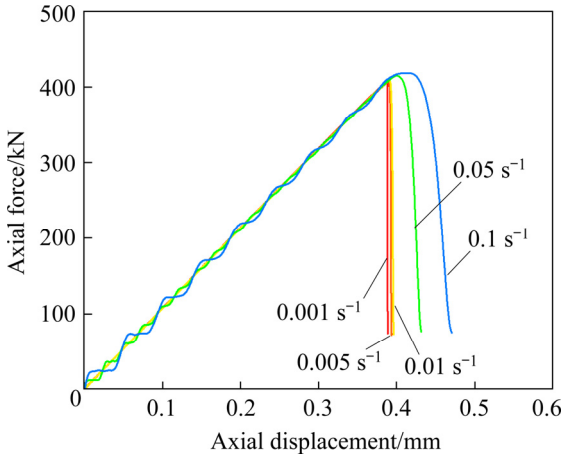

Fig. 8 Curves of normal contact force versus displacement with different strain rates

The peak stress was slightly higher with a larger particle spacing (Fig. 10). The section shape of the rock model is an approximate circle when the particle spacing is fine and an octagon when the particle spacing is coarse (Fig. 9). Consequently, stress concentrates at the sharp corners of the coarse particle model, causing higher normal stress. At the particle spacing of 1 mm, the modeled UCS (281.44 MPa; Fig. 10) is only 0.26% lower than the fitted UCS for Group M1 (282.18 MPa; Table 3). Thus, an SPH cylinder with the particle spacing of 1 mm was selected for UCS modeling.

4.4 Effect of time-step

The computational time-step strongly affects model accuracy and performance. Smaller steps generally improve accuracy but take longer to compute because there are more steps. Therefore, it is necessary to find the balance between simulation efficiency and accuracy. For a numerical model coupled with SPH and FEM, the time-step is governed by SPH rather than FEM. The SPH time-step, δt, varies according to the following equation:

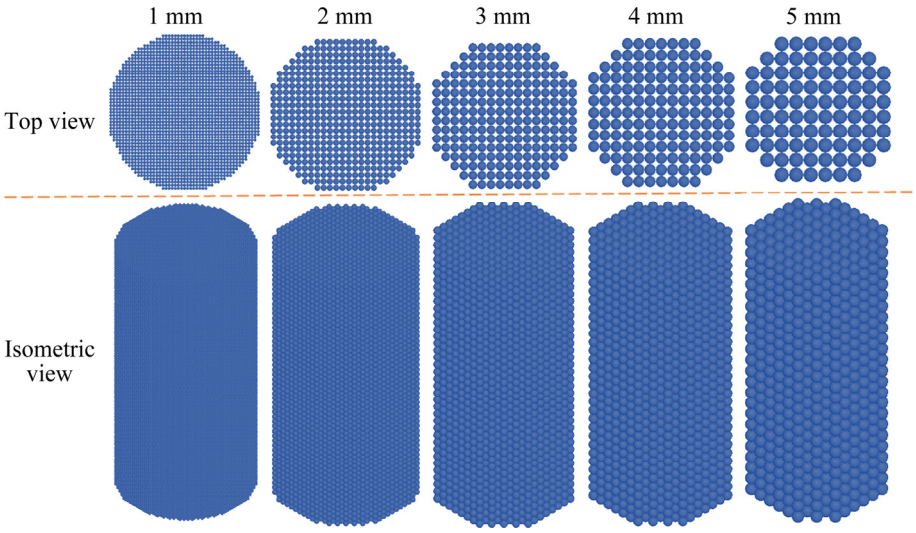

Fig. 9 SPH particle models with five particle spacings

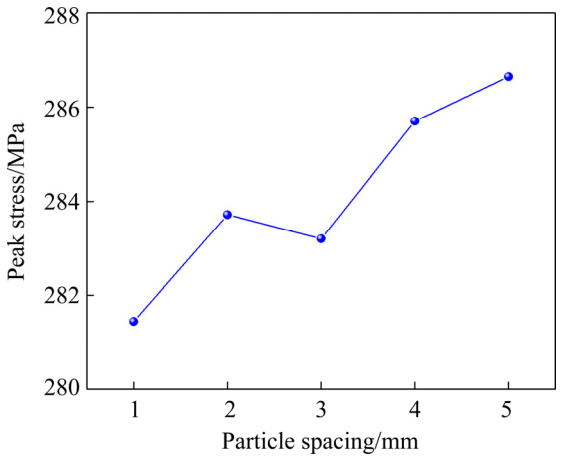

Fig. 10 Effect of particle spacing on peak stress

$$\delta t = C_{\mathrm{CFL}} \min_i \left(\frac{h_i}{c_i + v_i} \right) \tag{16}$$

where C_{CFL} is a numerical constant and h_i, c_i, and v_i denote the smoothing length, adiabatic speed of sound, and velocity of particle i.

In LS-DYNA, the scale factor TSSFAC (β') for computed time-step is introduced, which equals C_{CFL}. For a specific SPH model, β' is the only time-step parameter that can be defined by the user (without mass scaling). Except for the model time-step, the contact time-step also affects numerical results, which can be adjusted by changing contact stiffness and β'. The reasonable model time-step should not be greater than the minimum contact time-step. It is not recommended that β' is greater than 0.9 for stable calculation. Hence, β' was set to be 0.7, 0.8, and 0.9 to study the effect of time-step. The three resulting curves were virtually identical (Fig. 11). The normal contact forces of the three models were 522629, 522650, and 522637 N for β' of 0.7, 0.8, and 0.9, respectively. Given that time-step had almost no effect on UCS modeling results and taking computing time into consideration, the optimal time-step scale factor was determined to be 0.9.

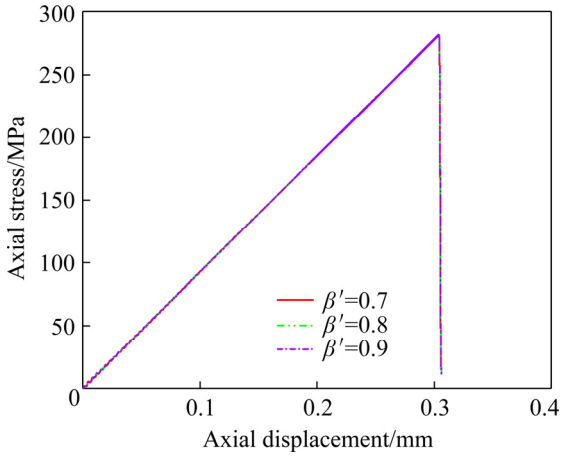

Fig. 11 Effect of three time-step scale factors on axial stress

4.5 Effect of particle approximation theory

The particle approximation theory is defined by the FORM value in the *CONTROL_SPH keyword. Among the 11 approximation theories in LS-DYNA R10, four are available for solid structures (0, 1, 7, and 8). In most solid structure applications, FORM 1 yields more accurate results around the boundary area. FORM 7 and FORM 8 provide the total Lagrangian formulation without

and with renormalization, respectively, which can help to avoid the tensile instability, but they are not applicable to large deformation analysis [40].

Approximation theories with renormalization (FORM 1 and FORM 8) yielded higher normal stress than FORM 0 and FORM 7 (Fig. 12). For FORM 0 or FORM 7, the numerical elastic modulus caused a large deviation when compared with the experimental elastic modulus, which indicated that the accuracy around the boundary area significantly affected the overall accuracy of the UCS model. In addition, approximation theories with renormalization have a longer computing time than those without renormalization. However, considering the accuracy of numerical results, employing the rock static strength simulation using SPH approximation theories with renormalization is suggested. Although FORM 8 can be used to avoid possible tensile instability, it cannot endure very larger deformations. Thus, FORM 1 was selected for UCS modeling.

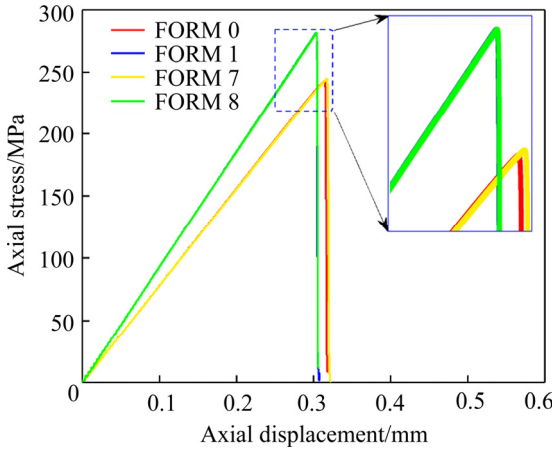

Fig. 12 Effect of particle approximation theory on normal stress

4.6 Effect of smoothing length

SPH elements consist of single node, and all element properties are centered on the single node. The initial smoothing length is constant for each part and is calculated as maximum value of all the minimum distance for each particle. Every SPH particle has its own smoothing length which varies in time based on Eq. (17):

$$\frac{\mathrm{d}}{\mathrm{d}t}h(t)=h(t)\nabla\cdot\boldsymbol{v} \tag{17}$$

where $h(t)$ is the smoothing length and $\nabla\cdot\boldsymbol{v}$ denotes the divergence of velocity vector.

The smoothing length is lower at high particle concentration than at low particle concentration: smoothing length varies to keep the same number of particles within its support domain. The smoothing length governed by Eq. (17) is scaled by CSLH in LS-DYNA code. It is recommended that the radius of the support domain governed by smoothing length covers more than two layers of SPH particles along each direction. SAKAKIBARA et al [41] tested CSLH values using the MAT_PLASTIC_KINEMATIC material model and concluded that a CSLH of 1.05 is most accurate. A CSLH >1.3 dramatically increases computing time. Thus, CSLH values between 1.05 and 1.3 are acceptable, and the default CSLH value is 1.2, which is applicable to most problems. CSLH values of 1.05, 1.2, and 1.3 were tested to assess the effect of smoothing length on UCS modeling.

CSLH values of 1.2 and 1.3 yielded similar peak stresses, whereas a CSLH of 1.05 yielded a lower peak stress (Fig. 13). Therefore, a CSLH value of 1.2 was chosen for UCS modeling.

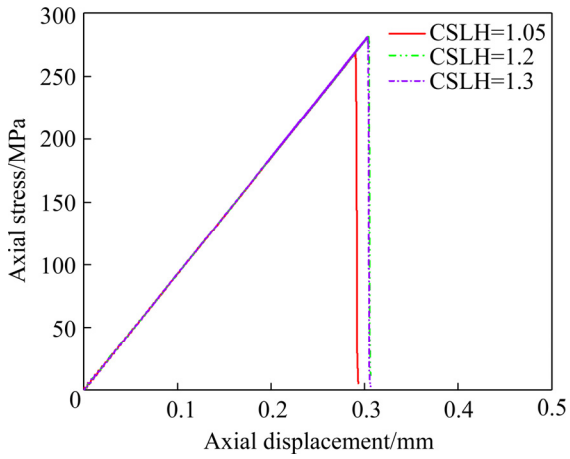

Fig. 13 Effect of smoothing length

In summary, based on parametric analysis, a nominal strain rate of 0.01 s^{-1}, time-step scaling factor of 0.9, particle approximation theory with FORM 1, smoothing length scaling factor of 1.2, and particle spacing of 1 mm were applied for all UCS modeling.

4.7 UCS modeling results

In experimental strength tests, microcracks induced by microwave exposure play significant roles in the rock failure mode. As mentioned before, the numerical modeling was based on the assumption that microwave-induced damage evenly

distributed in rock. Therefore, there is no comparability in the failure mode between numerical and experimental results. Figure 14 shows that the mechanical response differences of those specimens under different testing conditions are obvious. However, the rock failure modes are quite similar, and most specimens failed with X-shaped conjugate or multiple shear failure mode. In the UCS model of microwave-treated basalt, the post-peak stress curves decline dramatically and several cracks appear in a very short time, indicating that the model captures the brittle failure behavior of hard rock [42,43]. The maximum axial strains vary around 0.3%, which agrees with the experimental result of the study by LU et al [23]. This demonstrated that using experimental elastic modulus and Poisson's ratio ensured the deformation accuracy in the numerical results. Numerical results also indicated that elastic modulus and Poisson's ratio are consistent with experimental results. In addition, it is observed that the influences of microwave exposure time and power level on the rock strength and deformation characteristics in numerical simulation are consistent with experimental results. That is to say, the longer the microwave exposure time or the higher the microwave power level is, the more the reduction in rock strength is. The mean relative error between the modeled and fitted experimental UCS (Table 5) is 0.37%, indicating that selected SPH parameters work well for UCS modeling of microwave-treated basalt.

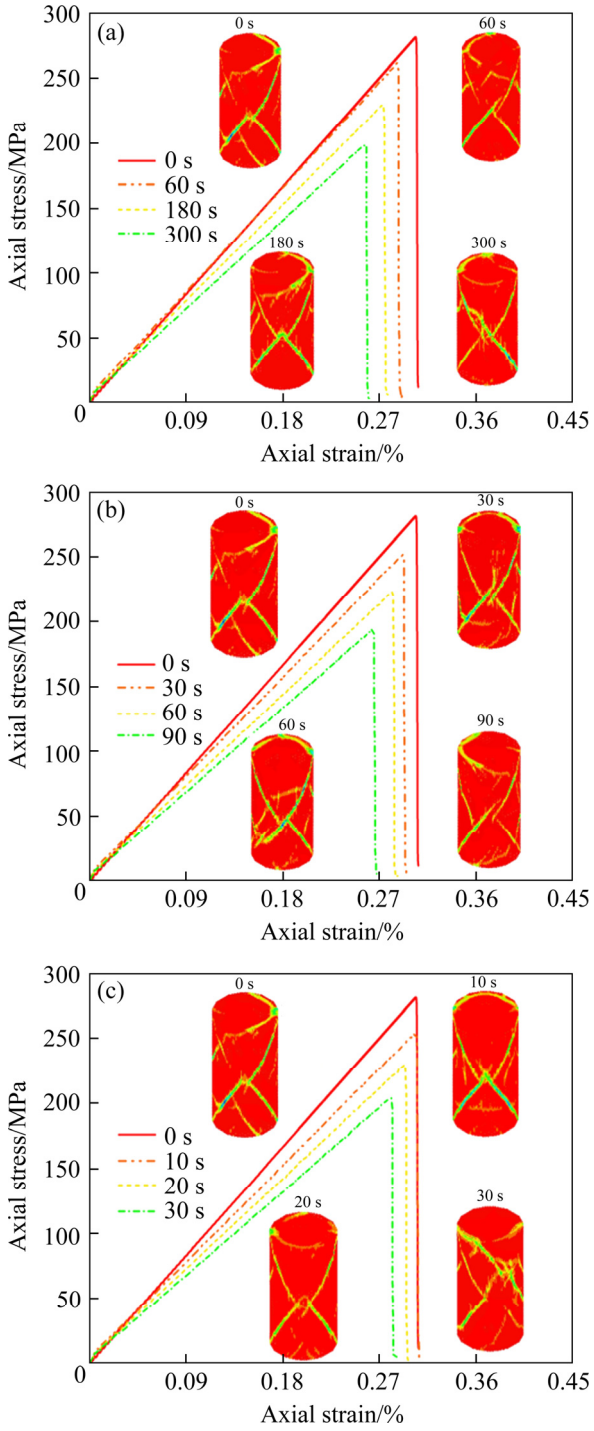

Fig. 14 Numerical stress versus strain curves and failure modes (distribution of effective plastic strain) of UCS modeling of basalt cylinders treated with microwaves at different power levels: (a) 1 kW; (b) 3 kW; (c) 5 kW

Table 5 Relative error between numerical and fitted experimental UCS data

Group	Fitted experimental UCS/MPa	Numerical UCS/MPa	Relative error/%
M1	282.18	281.44	0.26
M2	262.58	261.77	0.31
M3	231.38	230.54	0.36
M4	200.18	199.42	0.38
M5	253.08	252.23	0.34
M6	223.98	223.32	0.29
M7	194.88	194.45	0.22
M8	255.90	254.82	0.42
M9	231.00	229.87	0.49
M10	206.10	204.77	0.65

5 BTS modeling

5.1 Numerical boundary conditions

The BTS model is more sensitive to loading speed than the UCS model because the contact zone and specimen size differ. In order to eliminate the

oscillation in BTS modeling, the nominal strain rate was reduced to 0.001 s^{-1}, resulting in a longer computing time. Thus, based on the understanding that material mechanical behavior does not depend on model geometry, the rock model was created with a disc. It comprises two finite platens and one SPH disc (Fig. 15). The upper platen is applied at a constant vertical velocity and the lower platen is fixed.

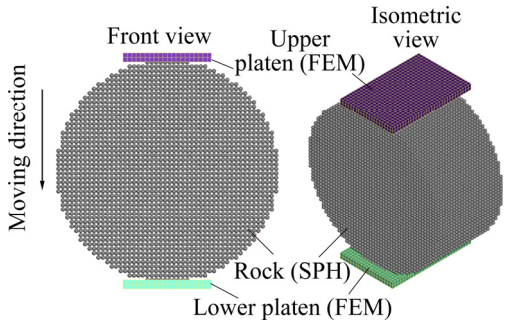

Fig. 15 Numerical model of BTS

5.2 Crack initiation and evolution

According to the plane elasticity theory and Griffith criterion, during BTS testing, a tensile crack should initiate at the center of the disc and then propagate along the compressive diametral line for homogeneous rock materials. The central crack initiation is captured by the SPH model (Fig. 16). The rock model is not a perfect circle in cross-section; therefore, the contact area between upper platen and rock specimen is rectangular, similar to the flattened Brazilian disc testing condition. In a flattened Brazilian disc test, the loading angle should not exceed 20° [44]. In this numerical model, the loading angle is 20°. Moreover, the flattened contact area contributes a larger compressive zone near the interface of platen and rock model than does the regular BTS test. Therefore, shear cracks occur at the two ends of the central crack and propagate to the edge of contact area. In addition, although stress concentrates slightly at the edge on the contact zone, it does not affect the central crack initiation.

5.3 BTS modeling results

The relative errors between numerical and fitted experimental BTS data are larger than those in the UCS model (Table 6). Even so, the largest difference between fitted experimental and numerical BTS is only 0.76 MPa (relative error is 4.88%).

Although the final crack distribution differed among BTS model, all cracks initiated along the loading diameter (Fig. 17). The initial compaction phase of stress versus displacement could not be captured by a homogeneous model. Therefore, the numerical displacement along the loading direction is less than the experimental value. The maximum vertical displacement of BTS numerical results ranges from 0.0142 to 0.0200 mm, whereas the

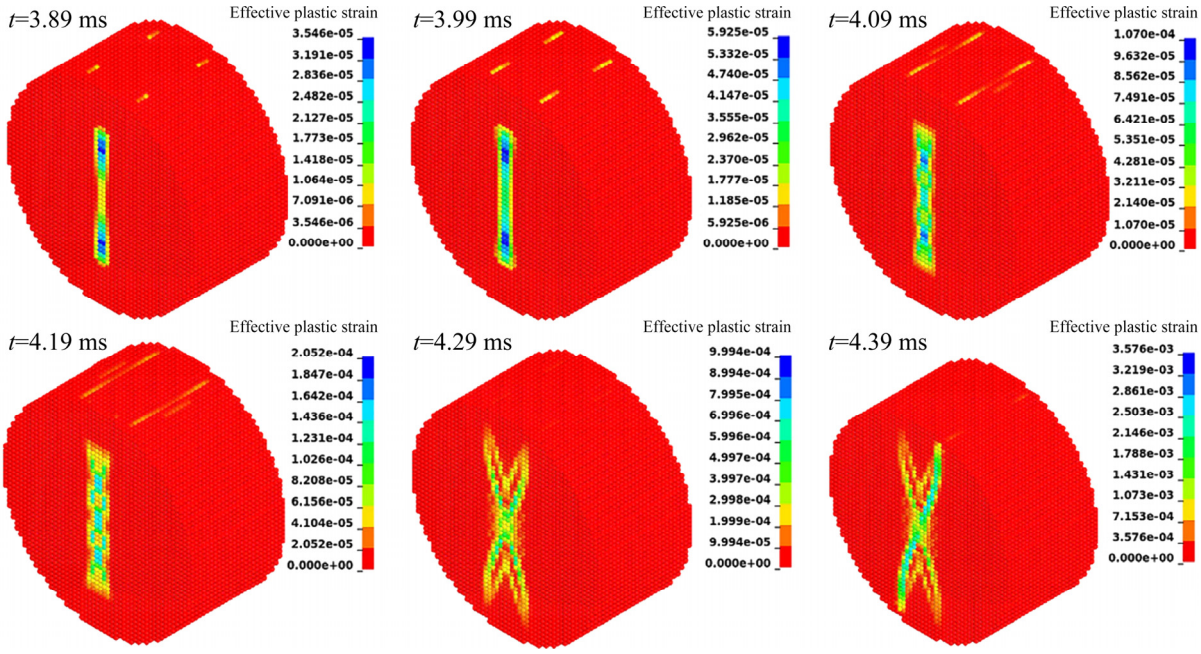

Fig. 16 Crack initiation and evolution during rock specimen failure in BTS testing (Group M1)

Table 6 Relative errors between numerical and fitted experimental BTS data

Group	Fitted experimental BTS/MPa	Numerical BTS/MPa	Relative error/%
M1	15.60	14.84	4.88
M2	14.40	13.86	3.77
M3	12.00	11.65	2.91
M4	9.60	9.42	1.83
M5	13.63	13.17	3.40
M6	11.83	11.48	2.97
M7	10.03	9.79	2.37
M8	12.99	12.64	2.67
M9	10.49	10.37	1.11
M10	7.99	8.07	1.02

maximum vertical displacement in experimental tests was 0.0800 mm, indicating that if the strain failure criterion is used for rock failure process simulation in LS-DYNA with a homogeneous model, it is necessary to calibrate the input data with experimental strain data.

6 Recommendations for future work

Since many challenges exist in measuring rock tensile strength using direct tensile strength (DTS) testing, indirect tests like BTS are widely used, though they tend to overestimate BTS relative to DTS results. Based on numerous experimental results, the relationship between DTS and BTS is given as DTS = fBTS, where f is approximately 0.9 for metamorphic, 0.8 for igneous, and 0.7 for sedimentary rocks [45]. Several BTS loading platen designs have been proposed to estimate the tensile strength of rock (e.g., flat platens with cushion, flat platens with small-diameter rods, or curved loading jaw), and the contact condition between the specimen and the steel platen could also influence BTS results. Except for rock breakage, the microwave treatment of rock is also assessed as a potential technology for rockburst prevention in deep hard rock engineering. The parametric study results presented in this work could provide an efficient approach for future numerical modeling on aforementioned technologies. However, to ensure the reliability of the rock mechanical parameters in subsequent research, the further calibration for the rock tensile strength is necessary.

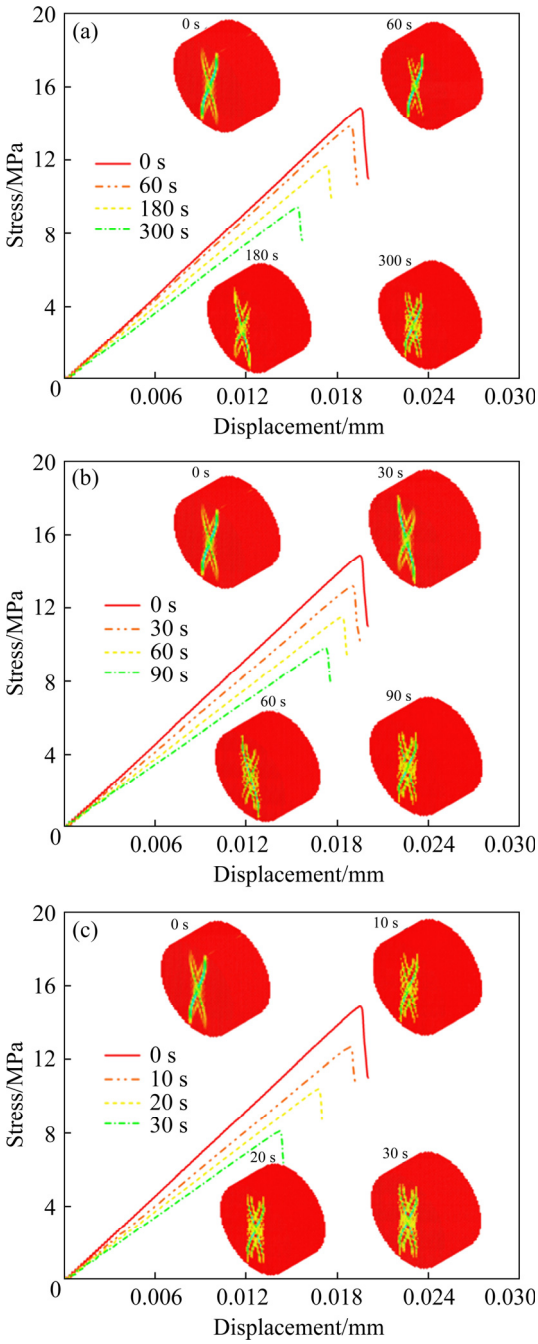

Fig. 17 Numerical stress versus displacement curves and failure modes of BTS modeling of basalt discs treated with microwaves at different power levels: (a) 1 kW; (b) 3 kW; (c) 5 kW

7 Conclusions

(1) A coupled SPH−FEM method is developed to simulate the UCS and BTS of microwave-treated basalt specimens. The mechanical parameters of cohesion and internal friction angle for microwave-treated basalt were calibrated according to linear Mohr−Coulomb theory. On the basis of parametric

sensitivity analysis of SPH simulation for UCS and BTS models, both UCS and BTS are captured simultaneously according to the same set of calibrated parameters.

(2) The attribution of evenly distributed SPH particles played a significant role in numerical results of a simulation involving cylinder- and disc-shaped model. In UCS modeling, coarse particle spacing generated sharp corner in the rock model, which led to stress concentration in the sharp corner and contributed to a higher UCS than expected. Due to the evenly distributed SPH particles, the numerical loading condition of BTS model was similar to a flattened Brazilian disc testing condition, which contributed to a larger compressive zone than a regular BTS model. The SPH particle spacing of the BTS model should be fine enough to make the loading angle less than 20°.

(3) The findings in this study lay the foundation for subsequent research such as numerical investigation of cutting or drilling performance for microwave-treated basalt. However, the rock mechanical parameters should be further calibrated based on experimental cutting and drilling results due to the difference between BTS and DTS. This is the focus of ongoing research.

Acknowledgments

Funding for this work was provided by the National Natural Science Foundation of China (No. 51774323), the Natural Science Foundation of Hunan Province, China (No. 2020JJ4704), and the Fundamental Research Funds for the Central Universities of Central South University, China (No. 2018zzts216). We thank the technical support regarding numerical simulation from Dr. Jerzy SALAMON, United States Bureau of Reclamation, Washington, D.C., United States and Dr. Benito MANZA. The first author also expresses his gratitude to the financial support from the China Scholarship Council and the support of the high-performance computer from Compute Canada. The Geomechanics Lab of McGill University contribution is acknowledged.

References

[1] ZHENG Y L, ZHAO X B, ZHAO Q H, LI J C, ZHANG Q B. Dielectric properties of hard rock minerals and implications for microwave-assisted rock fracturing [J]. Geomechanics and Geophysics for Geo-Energy and Geo-Resources, 2020, 6(1): 1−17.

[2] LU G M, LI Y H, HASSANI F, ZHANG X W. The influence of microwave irradiation on thermal properties of main rock-forming minerals [J]. Applied Thermal Engineering, 2017, 112: 1523−1532.

[3] WU B B, CHEN R, XIA K W. Dynamic tensile failure of rocks under static pre-tension [J]. International Journal of Rock Mechanics and Mining Sciences, 2015, 80: 12−18.

[4] LI X, WANG S, XU Y, YAO W, XIA K W, LU G M. Effect of microwave irradiation on dynamic mode-I fracture parameters of Barre granite [J]. Engineering Fracture Mechanics, 2020, 224: 106748.

[5] LI X, WANG S, XIA K W, TONG T Y. Dynamic tensile response of a microwave damaged granitic rock [J]. Experimental Mechanics, 2020, 61: 461−468.

[6] WANG S, XU Y, XIA K W, TONG T Y. Dynamic fragmentation of microwave irradiated rock [J]. Journal of Rock Mechanics and Geotechnical Engineering, 2020, 13(2): 300−310.

[7] HASSANI F, NEKOOVAGHT P. The development of microwave assisted machineries to break hard rocks [C]//The 28th International Symposium on Automation and Robotics in Construction. Seoul, South Korea, 2011: 678−684.

[8] HASSANI F, NEKOOVAGHT P M, GHARIB N. The influence of microwave irradiation on rocks for microwave-assisted underground excavation [J]. Journal of Rock Mechanics and Geotechnical Engineering, 2016, 8(1): 1−15.

[9] MEISELS R, TOIFL M, HARTLIEB P, KUCHAR F, ANTRETTER T. Microwave propagation and absorption and its thermo-mechanical consequences in heterogeneous rocks [J]. International Journal of Mineral Processing, 2015, 135: 40−51.

[10] HARTLIEB P, GRAFE B, SHEPEL T, MALOVYK A, AKBARI B. Experimental study on artificially induced crack patterns and their consequences on mechanical excavation processes [J]. International Journal of Rock Mechanics and Mining Sciences, 2017, 100: 160−169.

[11] ARORA S, KAUNDA R. New excavation technologies for underground construction: Linear cutting machine tests on microwave-irradiated granodiorite [R]. Department of Transportation. Office of the Assistant Secretary for Research and Technology. USA, 2018.

[12] YANG C, ZHOU K P, GAO R G, XIONG X. Numerical investigation of the dynamic response of a preconditioned roof in an underground mine: A case study of mining environment regeneration [J]. Soil Dynamics and Earthquake Engineering, 2021, 140: 106457.

[13] MARDALIZAD A, SAKSALA T, MANES A, GIGLIO M. Numerical modeling of the tool-rock penetration process using FEM coupled with SPH technique [J]. Journal of Petroleum Science and Engineering, 2020, 189: 107008.

[14] FAKHIMI A, LANARI M. DEM–SPH simulation of rock blasting [J]. Computers and Geotechnics, 2014, 55: 158−164.

[15] JONES D A, KINGMAN S W, WHITTLES D N, LOWNDES I S. Understanding microwave assisted breakage [J]. Minerals Engineering, 2005, 18(7): 659−669.

[16] NICCO M, HOLLEY E A, HARTLIEB P, PFAFF K. Textural and mineralogical controls on microwave-induced

cracking in granites [J]. Rock Mechanics and Rock Engineering, 2020, 53(10): 4745−4765.

[17] LU G M, SUN Z C, ZHOU J J, CHEN K, LI F Y. Effect of microwave irradiation on computed tomography and acoustic emission characteristics of hard rock [J]. Geotechnical and Geological Engineering, 2021, 39(1): 411−424.

[18] PAN Y C, LIU Q S, LIU J P, KONG X X, PENG X X, LIU Q. Investigation on disc cutter behaviors in cutting rocks of different strengths and reverse estimation of rock strengths from experimental cutting forces [J]. European Journal of Environmental and Civil Engineering, 2018, 29(6): 1−27.

[19] LUO Z Q, WEI W, QIN Y G, XIANG J. Early warning of rock mass instability based on multi-field coupling analysis and microseismic monitoring [J]. Transactions of Nonferrous Metals Society of China, 2019, 29(6): 1285−1293.

[20] LIU Z Z, CAO P, LIN H, MENG J J, WANG Y X. Three-dimensional upper bound limit analysis of underground cavities using nonlinear Baker failure criterion [J]. Transactions of Nonferrous Metals Society of China, 2020, 30(7): 1916−1927.

[21] SHEN Q Q, RAO Q H, LI Z, YI W, SUN D L. Interacting mechanism and initiation prediction of multiple cracks [J]. Transactions of Nonferrous Metals Society of China, 2021, 31(3): 779−791.

[22] LU G M, FENG X T, LI Y H, HASSANI F, ZHANG X W. Experimental investigation on the effects of microwave treatment on basalt heating, mechanical strength, and fragmentation [J]. Rock Mechanics and Rock Engineering, 2019, 52(8): 2535−2549.

[23] LU G M, FENG X T, LI Y H, ZHANG X W. Influence of microwave treatment on mechanical behaviour of compact basalts under different confining pressures [J]. Journal of Rock Mechanics and Geotechnical Engineering, 2020, 12(2): 213−222.

[24] GINGOLD R A, MONAGHAN J J. Smoothed particle hydrodynamics: Theory and application to non-spherical stars [J]. Monthly Notices of the Royal Astronomical Society, 1977, 181(3): 375−389.

[25] LUCY L B. A numerical approach to the testing of the fission hypothesis [J]. Astronomical Journal, 1977, 82: 1013−1027.

[26] LI H P, LI H J, QI L H, LUO J, ZUO H S. Simulation on deposition and solidification processes of 7075 Al alloy droplets in 3D printing technology [J]. Transactions of Nonferrous Metals Society of China, 2014, 24(6): 1836−1843.

[27] CAO W J, ZHOU Z Y, JIANG F M. Smoothed particle hydrodynamics modeling and simulation of foundry filling process [J]. Transactions of Nonferrous Metals Society of China, 2015, 25(7): 2321−2330.

[28] HE Y, ZHOU Z Y, CAO W J, CHEN W P. Simulation of mould filling process using smoothed particle hydrodynamics [J]. Transactions of Nonferrous Metals Society of China, 2011, 21(12): 2684−2692.

[29] LIU M, LIU G. Smoothed particle hydrodynamics (SPH): An overview and recent developments [J]. Archives of computational methods in engineering, 2010, 17(1): 25−76.

[30] LIBERSKY L D, PETSCHEK A G, CARNEY T C, HIPP J R, ALLAHDADI F A. High strain Lagrangian hydrodynamics: A three-dimensional SPH code for dynamic material response [J]. Journal of Computational Physics, 1993, 109(1): 67−75.

[31] MAO Z R, LIU G R, DONG X W. A comprehensive study on the parameters setting in smoothed particle hydrodynamics (SPH) method applied to hydrodynamics problems [J]. Computers and Geotechnics, 2017, 92: 77−95.

[32] VERMA A S, CASTRO S G P, JIANG Z Y, TEUWEN J J E. Numerical investigation of rain droplet impact on offshore wind turbine blades under different rainfall conditions: A parametric study [J]. Composite Structures, 2020, 241: 112096.

[33] BIENIAWSKI Z T, BERNEDE M J. Suggested methods for determining tensile strength of rock materials [J]. International Journal of Rock Mechanics and Mining Sciences, 1978, 15(3): 99−103.

[34] HALLQUIST J O. LS-DYNA keyword user's manual [M]. California, USA: Livermore Software Technology Corporation, 2007: 299−800.

[35] SHANG J, HENCHER S R, WEST L J. Tensile strength of geological discontinuities including incipient bedding, rock joints and mineral veins [J]. Rock Mechanics and Rock Engineering, 2016, 49(11): 4213−4225.

[36] KONESHWARAN S, THAMBIRATNAM D P, GALLAGE C. Blast response of segmented bored tunnel using coupled SPH−FE method [J]. Structures, 2015, 2: 58−71.

[37] YANG C, HU J H, MA S W. Numerical investigation of rock breaking mechanism with supercritical carbon dioxide jet by SPH-FEM approach [J]. IEEE Access, 2019, 7: 55485−55495.

[38] XIE L X, YANG S Q, GU J C, ZHANG Q B, LU W B, JING H W, WANG Z L. JHR constitutive model for rock under dynamic loads [J]. Computers and Geotechnics, 2019, 108: 161−172.

[39] ZHOU X P, YANG H Q. Micromechanical modeling of dynamic compressive responses of mesoscopic heterogenous brittle rock [J]. Theoretical and Applied Fracture Mechanics, 2007, 48(1): 1−20.

[40] GIANNAROS E, KOTZAKOLIOS A, KOSTOPOULOS V, CAMPOLI G. Hypervelocity impact response of CFRP laminates using smoothed particle hydrodynamics method: Implementation and validation [J]. International Journal of Impact Engineering, 2019, 123: 56−69.

[41] SAKAKIBARA T, TSUDA T, OHTAGAKI R. A study of quasi-static problem by SPH method [C]//10th International LS-DYNA Users Conference. Detroit, 2008.

[42] LI Z, RAO Q H, LI P, YI W. Crack initiation rate of brittle rock under thermal-hydro-mechanical coupling condition [J]. Transactions of Nonferrous Metals Society of China, 2018, 28(10): 2107−2113.

[43] YI W, RAO Q H, LI Z, SHEN Q Q. A new measurement method of crack propagation rate for brittle rock under THMC coupling condition [J]. Transactions of Nonferrous Metals Society of China, 2019, 29(8): 1728−1736.

[44] LIN H, XIONG W, YAN Q X. Modified formula for the tensile strength as obtained by the flattened Brazilian disk test [J]. Rock Mechanics and Rock Engineering, 2016, 49(4): 1579−1586.

[45] PERRAS M A, DIEDERICHS M S. A review of the tensile strength of rock: Concepts and testing [J]. Geotechnical and Geological Engineering, 2014, 32(2): 525−546.

微波处理玄武岩强度的 SPH−FEM 耦合算法模拟

杨 春[1,2,3]，Ferri HASSANI[2]，周科平[1,3]，高 峰[1,3]，Ameen TOPA[4,5]

1. 中南大学 资源与安全工程学院，长沙 410083；
2. Department of Mining and Materials Engineering, McGill University,
3450 University, Frank Dawson Adams Bldg., Montreal, QC H3A 0E8, Canada;
3. 中南大学 高海拔寒区采矿工程技术研究中心，长沙 410083;
4. Institute of Transportation Infrastructure, Universiti Teknologi PETRONAS, Seri Iskandar, Perak 32610, Malaysia;
5. Department of Maritime Technology, University Malaysia Terengganu, Kuala Terengganu 21300, Malaysia

摘 要：微波预处理弱化岩体强度，进而降低机械破岩过程中的钻头/刀具磨损、提升凿岩效率已经成为一项极具前景的技术。为探究数值模拟参数对岩石静强度模拟结果的影响，并为后续钻凿或岩石切割模拟确定合理的微波处理玄武岩数值力学参数，采用光滑粒子流体动力学与有限元耦合算法(SPH−FEM)构建岩石单轴压缩与巴西拉伸数值模型。为减小微波损伤对岩石强度测试误差的影响，采用线性莫尔−库仑理论对相同微波参数下微波处理玄武岩试样的黏聚力和内摩擦角进行标定。在单轴抗压与巴西拉伸模拟过程中开展 SPH 关键控制参数的敏感性分析，并根据同一组校核后的黏聚力和内摩擦角数据，在数值实验中同时捕获目标抗压强度与巴西拉伸强度，单轴抗压强度数值模拟结果与试验结果吻合较好。此外，结合数值模拟结果评估微波辐照参数对玄武岩力学行为的影响。

关键词：微波照射；微波辅助破岩；岩石力学；光滑粒子流体动力学(SPH)；参数敏感性分析

(Edited by Bing YANG)